

Super-resolution reconstruction in ultrahigh-field MRI

Macy Payne,^{1,2} Ivina Mali,¹ Thomas Mueller,³ Mary Cain,⁴ Ronen Segev,⁵ and Stefan H. Bossmann^{2,*}

¹Department of Chemistry, Kansas State University, Manhattan, Kansas; ²Department of Cancer Biology, The University of Kansas Medical Center, Kansas City, Kansas; ³Department of Biology, Kansas State University, Manhattan, Kansas; ⁴Department of Psychological Sciences, Kansas State University, Manhattan, Kansas; and ⁵Life Sciences Department, Ben Gurion University of the Negev, Beer Sheva, Israel

ABSTRACT Magnetic resonance imaging (MRI) is a highly significant imaging platform for a variety of medical and research applications. However, the low spatiotemporal resolution of conventional MRI limits its applicability toward rapid acquisition of ultrahigh-resolution scans. Current aims at high-resolution MRI focus on increasing the accuracy of tissue delineation, assessments of structural integrity, and early identification of malignancies. Unfortunately, high-resolution imaging often leads to decreased signal/noise (SNR) and contrast/noise (CNR) ratios and increased time cost, which are unfeasible in many clinical and academic settings, offsetting any potential benefits. In this study, we apply and assess the efficacy of super-resolution reconstruction (SRR) through iterative back-projection utilizing through-plane voxel offsets. SRR allows for high-resolution imaging in condensed time frames. Rat skulls and archerfish samples, typical models in academic settings, were used to demonstrate the impact of SRR on varying sample sizes and applicability for translational and comparative neuroscience. The SNR and CNR increased in samples that did not fully occupy the imaging probe and in instances where the low-resolution data were acquired in three dimensions, while the CNR was found to increase with both 3D and 2D low-resolution data reconstructions when compared with directly acquired high-resolution images. Limitations to the applied SRR algorithm were investigated to determine the maximum ratios between low-resolution inputs and high-resolution reconstructions and the overall cost effectivity of the strategy. Overall, the study revealed that SRR could be used to decrease image acquisition time, increase the CNR in nearly all instances, and increase the SNR in small samples.

WHY IT MATTERS Ultrahigh-resolution magnetic resonance imaging is critical for increasing the understanding of a variety of biological systems. It is a noninvasive strategy that can be repeated to follow the progression of diseases, monitor growth over broad time frames, and extract a variety of quantitative parameters to monitor tissue structure, organization, and health. Unfortunately, ultrahigh-resolution imaging comes with increased time costs and low signal/noise and contrast/noise ratios and is often limited by the overall instrument strength available. Super-resolution reconstruction is a rapidly growing area that allows for ultrahigh-resolution imaging at clinical strengths, increasing image clarity in the process. Throughout this article, we assess the validity of the results gained from the application of super-resolution reconstruction and illustrate the benefits and limitations across various samples.

INTRODUCTION

Ultrahigh-field magnetic resonance imaging (MRI) is increasingly attentive to its overall safety toward its application in clinical settings. Instrumentation up to 8 T is considered reasonably safe for human subjects older than infancy, and prolonged exposure has been shown to have nominal, if any, impacts (1). Reported side effects were short lived, and homeostasis was achieved within minutes postimaging (2). Additionally,

most complaints regarding imaging from human subjects did not pertain to “true” side effects in the sense that they were caused by the magnetic field (3) and instead were related to general discomfort caused by the noise during imaging and the length of imaging time requiring subjects to remain motionless throughout the procedure. Some discomfort can be circumvented through headphones and attempts to condense imaging time through parameter optimization and assessing the key factors most important for diagnosis. While moving toward ultrahigh-field MRI is a great step toward increasing the depth, accuracy, and precision of information capable of being derived from a multitude of acquisition series, there

Submitted November 15, 2022, and accepted for publication March 22, 2023.

*Correspondence: sbossmann@kumc.edu

Editor: Paul Schanda.

<https://doi.org/10.1016/j.bpr.2023.100107>

© 2023 The Author(s).

This is an open access article under the CC BY-NC-ND license (<http://creativecommons.org/licenses/by-nc-nd/4.0/>).



TABLE 1 SNR and CNR values for reconstructed image of archerfish brain and directly acquired high-resolution image.

Image type	SNR	CNR
Reconstructed high res. image	8.487	7.428
Directly acquired high res.	6.171	5.000

are some inherent drawbacks as well. Cost is a dominating factor in procuring new high-field instrumentation, and ultrahigh fields have yet to become common in clinical settings, although they have slowly been integrated in some locations. Thus, while obtaining ultrahigh-resolution images in ultrahigh-fields with high signal/noise ratios (SNRs) are the gold standard for MRI, alternative methods must be investigated to obtain access to higher-resolution imaging even at clinical field strengths of 1.5–3 T.

Resolution, within the context of MRI, is the spatial resolution pertaining to the voxel sizes used throughout imaging. It is determined by the matrix size and field of view and, in combination with the SNR and the contrast/noise ratio (CNR), will impact the ability to delineate between different structures (4,5). Spatial resolution is a key component to imaging that denotes the size of the voxels, with smaller voxels being less prone to partial volume effects but often

suffering from lower SNRs. This can make the final images noisy and difficult to read due to low signal per voxel. Increasing the spatial resolution based on imaging parameters alone, such as repetition times (TRs), echo times (TEs), fields of view (FOVs), and matrix sizes, is limited in a few different aspects. In particular, the FOV is limited by probe size and gradient strength, and increasing the matrix in the phase-encoding dimension comes at the cost of dramatic scan time increases (6). Consequently, acquiring ultrahigh-resolution images can be difficult and costly. To circumvent the high cost with ultrahigh-resolution imaging, an emerging area of super-resolution reconstruction offers a potential method to increase the accessibility to high-spatial-resolution images (6–15). Super-resolution reconstruction (SRR) is a method that involves acquiring multiple low-resolution images at a series of offsets within the matrix in the phase-encoding, frequency-encoding, or slice direction (11). It decreases the time costs associated with high-resolution data sets and offers the potential for higher SNRs, as well, due to the increased signal in the images used in the reconstruction. Conversely, zero padding and zero filling are alternative methods that can be used to increase the resolution artificially and will generate a higher-resolution final image while reducing the overall

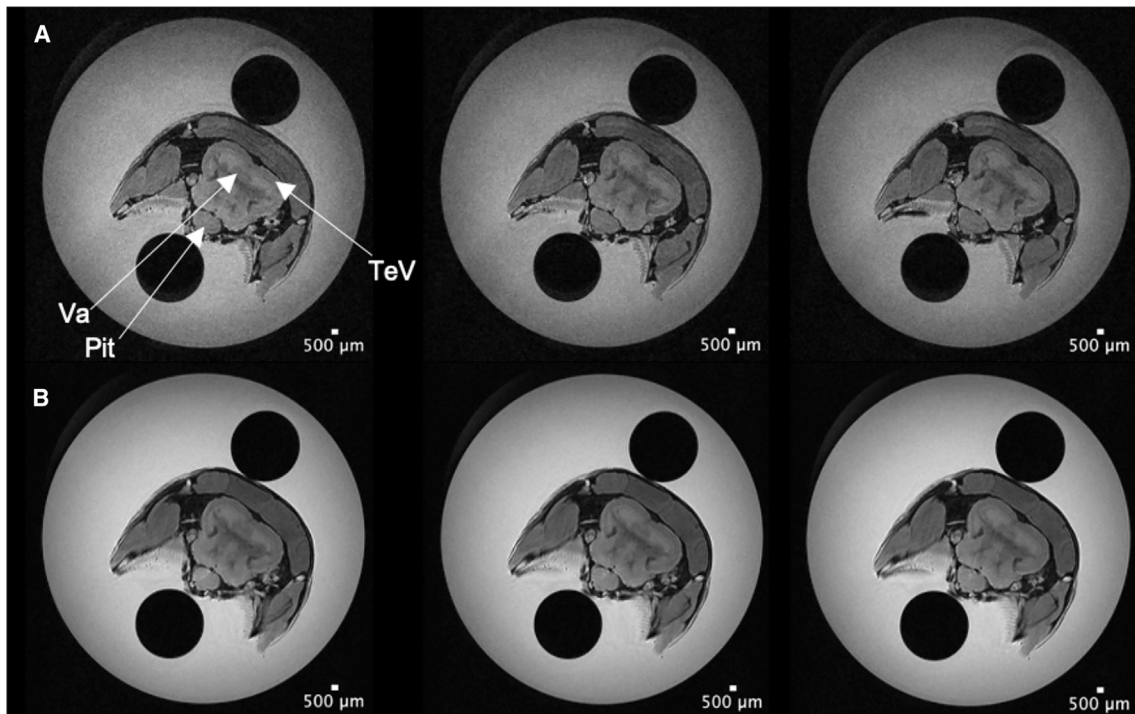


FIGURE 1 Archerfish high-resolution and reconstructed high-resolution images. Comparison across three slices of the directly acquired high-resolution images (row A) and the reconstructed high-resolution volume (row B) for the archerfish brain. The directly acquired high-resolution image has increased noise as seen by the “salt and pepper” appearance of the background, making it more difficult to assess anatomical structures, while the reconstructed volume demonstrates decreased background noise as well as increased contrast between anatomical regions. Anatomical regions are denoted in the first top left figure, illustrating regions of the valvula cerebelli, pituitary, and tectal ventricle.

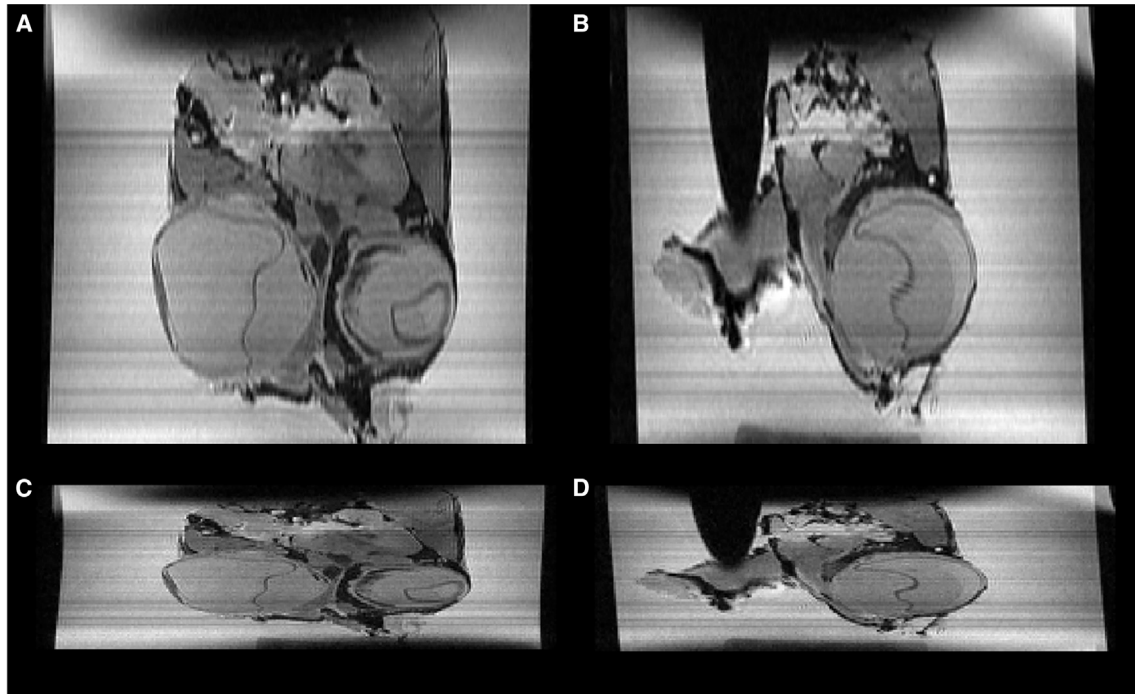


FIGURE 2 Sagittal and coronal views of the archerfish brain. (A) and (B) demonstrate the preservation of anatomical structures and image integrity after super-resolution reconstruction to isotropic voxel sizes. (C) and (D) demonstrate the distortions present with the low-resolution data sets, making it difficult to decipher anatomical structures.

time cost. However, they do not generate true signal information at these zero-filled or zero-padded voxels.

Among current methods of spatial resolution enhancements, zero padding and zero filling are often the only ones readily equipped with the instruments. One way of using these methods involves padding the matrix with zeros along the border of the matrix, increasing the overall matrix size. Filling these regions with zeros condenses the acquisition time and in-

creases the matrix size to prevent the “thinning” of voxels in the phase-encoding dimension. This procedure, therefore, reduces the overall pixelation of the image, resulting in an artificially increased spatial resolution without adding new information. Alternatively, zero filling can be used to fill regions of k-space with zeros where information between regions of data acquired is interpolated to fill the unknown signal based upon the signals of the neighboring voxels

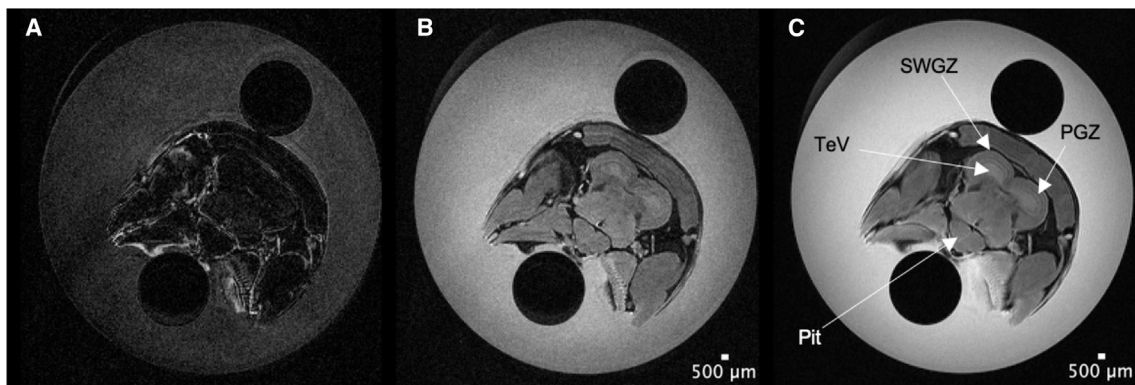


FIGURE 3 Archerfish image reconstruction assessment. (A) The absolute difference between the high-resolution image directly acquired at 14 T. (B) The slice of the high-resolution image taken for analysis. (C) The corresponding slice of the reconstructed image. (A) details the loss of background noise from the reconstruction compared with the high-resolution image that was directly acquired. This is due to the increased SNR seen in (C) while maintaining a high degree of anatomical accuracy in the reconstruction. The decrease in noise in (C) also makes it possible to discriminate between different regions of the brain lost due to the decreased SNR in (B). Anatomical markers are denoted with white arrows outlining the pituitary, tectal ventricle, superior white and gray zone of the optic tectum, and the periventricular gray zone of the optic tectum.

TABLE 2 SNR and CNR comparison of image reconstruction with varying numbers of low-resolution inputs.

Number of images for reconstruction	SNR	CNR
3	15.593	6.959
4	16.431	7.000
6	21.752	8.723
12	28.830	11.533

(5,16,17). Overall, zero padding and zero filling do not generate any new information about the regions where signals were not originally acquired/sampled and instead are methods to reduce pixelation and improve acquired spatial resolution based upon the additional clarity in the final images.

Alternatively, SRR, based upon modeling the image process, can produce new images at increased spatial resolution based upon a series of data sets acquired at low spatial resolutions (6,12,18). While SRR is not a novel technique, it has recently gained a high degree of focus from the imaging community. There are a variety of methods in which to employ SRR, from neural networks to a variety of algorithms that utilize low-resolution (LR) inputs to reconstruct a high-resolution (HR) image (8,9,15,19). The predominant focus of this study was to utilize the basic idea that low-spatial-resolution images acquired at an offset

contribute new, unknown information to the previous data set acquired that can be estimated and used to generate higher-spatial-resolution data sets and assess the accuracy of the HR estimate against directly acquired counterparts for scans acquired with rapid imaging with refocused echo pulse sequences (rapid acquisition with refocused echo [RARE]). The image modeling operates upon known geometric information to estimate the HR images, which are then used to predict the expected LR images. The error between the estimated LR data set and the acquired LR data set is minimized to improve the estimate for the final HR image (12,18).

Here, we applied iterative back projection to perform SRR for conventional RARE sequences that allows for higher-spatial-resolution images without compromising scan time. To directly compare the loss of the super-resolution techniques when applied to RARE imaging sequences, directly acquired HR images are also obtained at ultrahigh-field strengths of 14 T to measure any deviations from the anatomical structures within the subjects of interest. Furthermore, the impact on the number of LR data sets was briefly examined along with the acquisition of LR images in 2D and 3D and their impacts to the SNRs and CNRs of the reconstructed images.

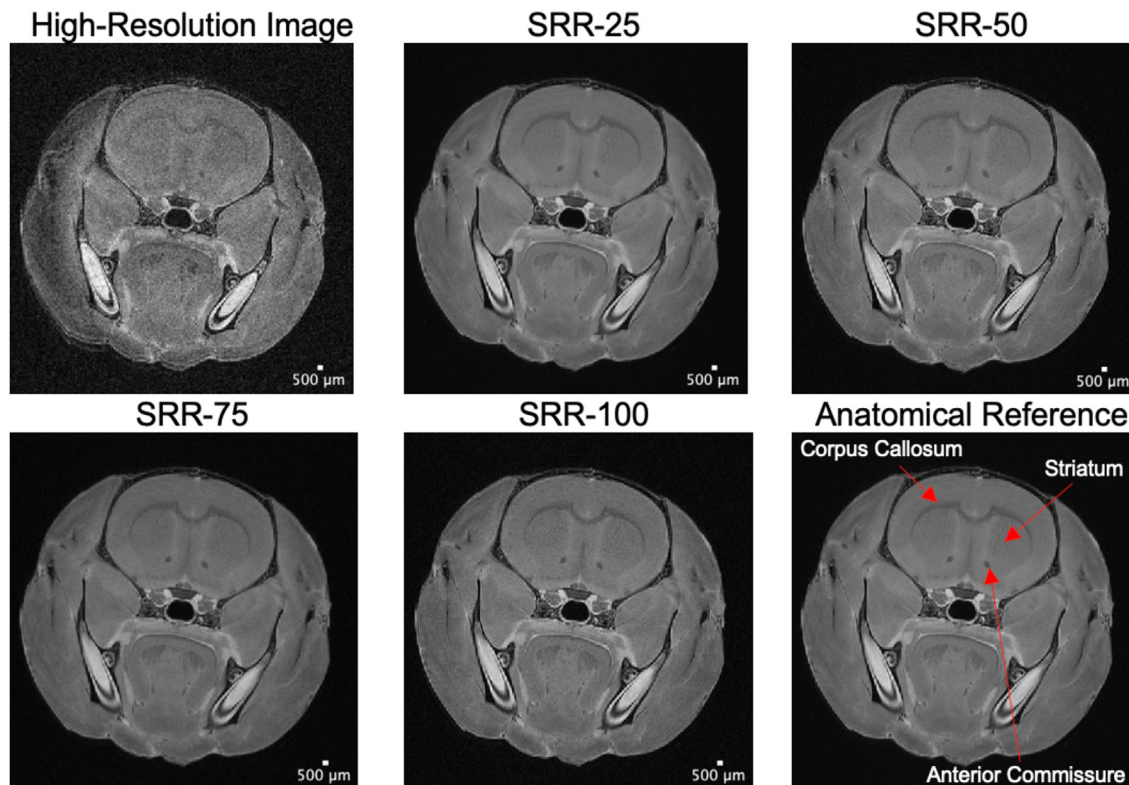


FIGURE 4 Reconstructed images from 3D low-resolution data. Images of the corresponding slices between the high-resolution image directly acquired and then various reconstructions. SRR-# indicates the offset between the low-resolution inputs, with a larger number indicating fewer low-resolution inputs used in the reconstruction. An additional image is labeled with three anatomical regions for reference.

We applied this method to the brains of both rats and archerfish because of several aspects that made them useful for assessing SRR. First, rats are an established model system for human neurological disorders and have been widely used for research (20,21). Their brains are also large enough to perform physiological experiments in live animals under conventional MRI settings, that is, these experiments on rats are highly comparable to those used for human patients in clinical settings. Moreover, standard rat atlases are available (22–25), making rats a perfect choice for testing new imaging methods like SRR. Archerfish, which have a recently published brain atlas (26), are becoming an increasingly important model for brain research because of their specialized hunting mode (27,28). These fish shoot down insects above the water surface with high precision and therefore have evolved a highly effective visual system including a more pronounced optic tectum located in the dorsal midbrain. Improving high-spatial-resolution MRI with SRR represents an attractive option for enhancing imaging possibilities that are currently limited to larger specimens only. In other words, by applying SRR to MRI of archerfish, we aim to improve existing MRI methodologies for

specimens that, compared with rats and other mammals, have a somewhat disadvantaged brain/body ratio such that their brains are relatively smaller compared with the rest of the body. Close comparisons between rats and archerfish, therefore, are very informative for developing enhanced high-spatial-resolution MRI methodologies, which is the objective of this study. In addition, the application of the new methodology to two animal models that are evolutionary distant, like rats and archerfish, gives hope that this technique will be applicable to a wide range of specimens.

MATERIALS AND METHODS

Imaging archerfish

Recently, archerfish have been studied in the context of their peculiar lifestyle and feeding habits, especially their ability to shoot down their prey, and in applications in learning about visual processing in species with no cortex (27,28). Unfortunately, imaging small samples, such as the archerfish brain, can make it difficult to achieve high spatial resolution with reasonable SNRs. This is due to the increased distance between the subject and the transmitter and receiver coils leading to a depressed SNR. Additionally, to obtain high spatial resolutions, matrix sizes must increase correspondingly due to the high level of tissue variation within a small region, which

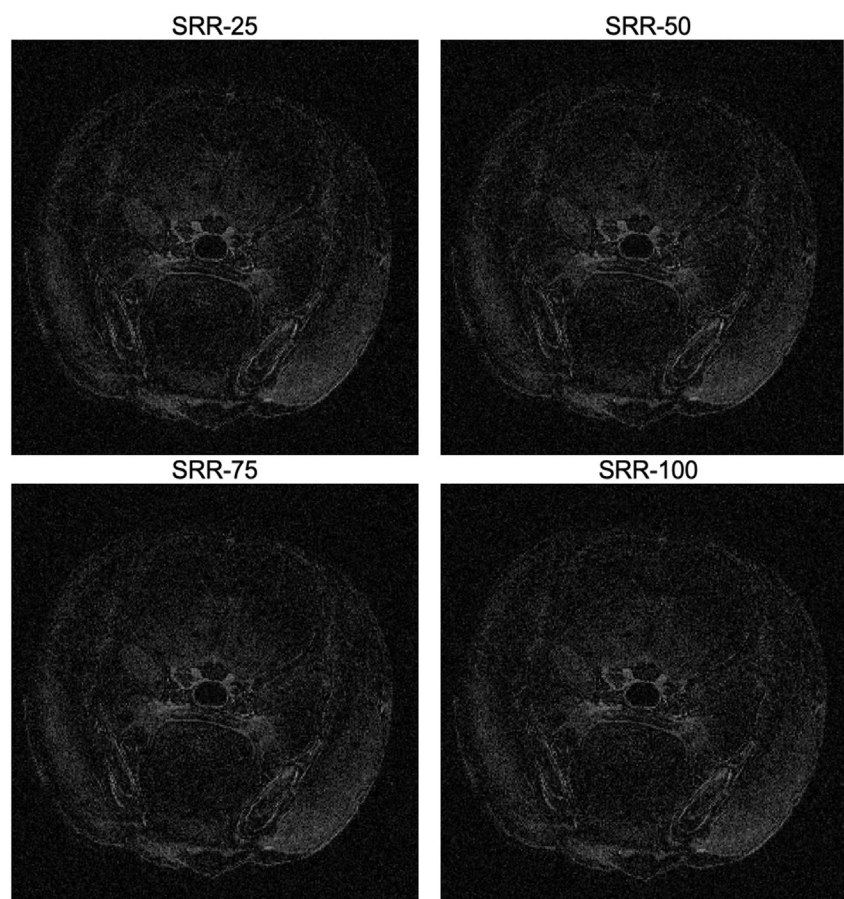


FIGURE 5 Reconstruction quality assessment from 3D low-resolution data. The absolute differences between the reconstructed images with offsets of 25, 50, 75, and 100 μm and the directly acquired high-resolution images. The image depicts the large volume of noise that is excluded from the reconstructed images as seen by the salt and pepper noise throughout the images difference.

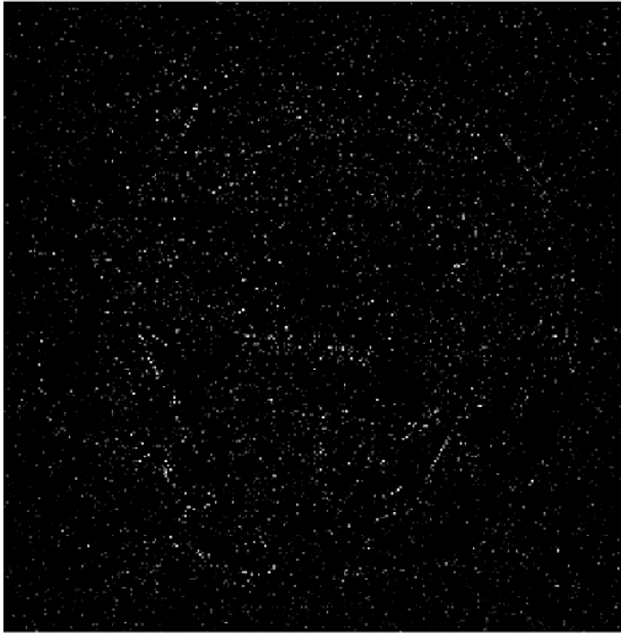


FIGURE 6 Noise removed with increased quantity of low-resolution inputs. Difference between the 25 μm reconstruction and the 100 μm reconstruction offsets with varying numbers of low-resolution inputs demonstrating the increased noise in the 100 μm reconstruction strategy that is excluded from the 25 μm offset reconstructions.

decreases the signal per voxel further, exacerbating the SNR dilemma. Therefore, an archerfish brain was used as our initial subject of investigation for the use of SRR as it represents an important subject in neuroscience research while also presenting with a key complication seen in MRI. A perfused and fixed archerfish brain was placed within a 20 mm glass tube and filled with phosphate buffer solution and imaged in a 30 mm diameter probe. Anatomical imaging was performed four times to acquire axial slices using a T_2 RARE imaging sequence with a TR/TE of 2500/30.22 ms, a RARE factor of 16, 2 averages, and a matrix size of 256×256 . One image acquisition series focused on acquiring the HR data set directly with a spatial resolution of $100 \times 100 \times 100 \mu\text{m}$ for a total scan time of 5 h and 41 min. The remaining LR images were acquired with a spatial resolution of $100 \times 100 \times 300 \mu\text{m}$ and a through-plane offset of 100 μm for a total imaging time of 1 h and 53 min per data set. Images were acquired in 3D to keep duty cycles low and with enough slices to cover the full sample length from olfactory bulb to the end of the cerebellum.

Imaging rat brains

In translational and comparative neuroscience, rats serve as proxies for human neurological and psychiatric disorders, assist in the study of cancer progression, and lend themselves to more flexible interventions than their alternative small-animal counterparts (21). For this reason, rat brains were also imaged, as they are frequent subjects of study in translational research examining connectivity and other brain formations to grasp a deeper understanding of complex pathologies. Ex vivo rat brains were imaged immersed in Fomblin in a 28 mm flat bottom glass MRI tube and imaged in a 30 mm diameter probe.

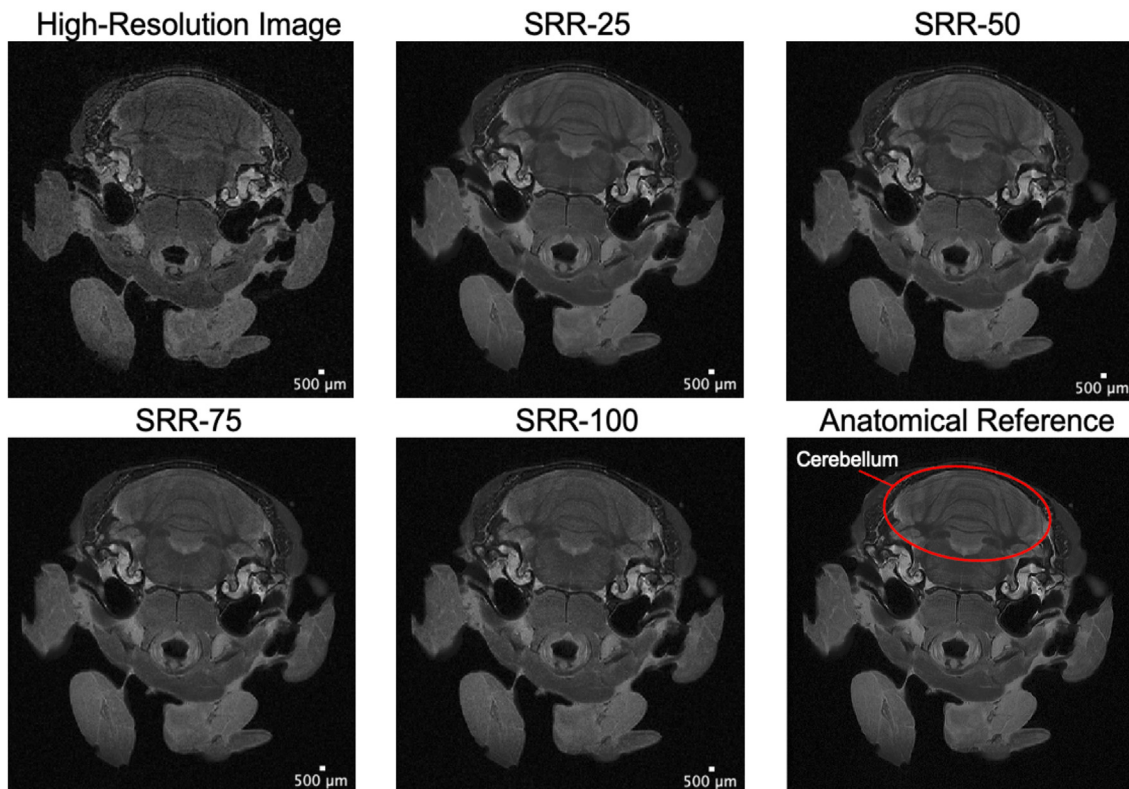


FIGURE 7 Reconstructed cerebellum images from 3D low-resolution inputs. Selected slices of the rat cerebellum from high-resolution and reconstructed data sets for reconstruction accuracy measurements. Image headers denote the image type (high resolution directly acquired and super-resolution reconstruction) and the offset used in collecting the low-resolution data sets.

Imaging parameters were as follows: TR/TE = 2500/22 ms, RARE factor of 10, 1 average, a matrix size of 289×289 , and a slice thickness of $300 \mu\text{m}$ for the LR data sets, with 12 data sets acquired with $25 \mu\text{m}$ offsets in the slice selection direction. The scan time was 1 h and 29 min and 50 s per LR data set, or 17 h and 58 min for all 12 LR data sets. The HR data set was acquired with 12 averages and a slice thickness of $100 \mu\text{m}$ for a spatial resolution of $100 \times 100 \times 100 \mu\text{m}$ and would have taken 53 h and 54 min to acquire. To maintain a reasonable time frame, fewer slices were acquired (from over 200 to 10) to condense imaging time to 25 h.

An additional iteration involved using 2D LR data sets to reconstruct the 3D HR acquired image. To maintain a reasonable duty cycle of under 10%, slices were condensed to 10 slices for a slice thickness of $300 \mu\text{m}$ for the LR data set, and the RARE factor was decreased to 6. TRs and TEs were 2500 and 22.45 ms for both LR and HR data sets, and an average of 2 was used in the LR acquisition. Slice offsets of $50 \mu\text{m}$ were used to generate two possible reconstructions. Imaging time for the LR data sets was 4 min and 5 s, for a total of 24 min and 30 s for the full LR data set acquisition of six separate image series. A comparable 3D HR data set was acquired directly with $100 \mu\text{m}$ isotropic spatial resolution across 30 slices with 12 averages for a total imaging time of 12 h.

In order to determine at which point the SRR technique no longer captures the information between successive steps, or the point at which the information gained is no longer sufficient to reconstruct the higher-resolution goal, the 2D LR images were again acquired with 400, 500, and $600 \mu\text{m}$ slice thickness. The imaging parameters changed slightly depending upon the slice thickness. The 400 and $500 \mu\text{m}$ data sets were acquired with a TR/TE of 2500/11 ms and a RARE factor of 4 for a total imaging time of 3 min. The $600 \mu\text{m}$ data set was acquired with a TR/TE of 2500/22.45 ms and a RARE factor of 6. An additional HR data set was acquired with a TR/TE of 2500/16 ms and a RARE factor of 6 for the 400 and $500 \mu\text{m}$ data sets, with $100 \mu\text{m}$ isotropic spatial resolution to obtain the echo at the shortest available time point as was done for the 400 and $500 \mu\text{m}$ data sets. Each image series was performed with a 100 and $50 \mu\text{m}$ offset to perform two reconstructions with varying levels of LR inputs. Then, the SRR iterative back projection was used to reconstruct $100 \mu\text{m}$ isotropic spatial resolution data sets, and the SNR, CNR, and absolute difference between the reconstructed HR image and the directly acquired HR image were determined.

Instrumentation

All imaging was performed on a Bruker WB 600 MHz (14 T) MRI with an exchangeable MICWB40 probe. The 30×40 mm radiofrequency coil was used throughout all imaging. Imaging software to control parameter input was Paravision 6.0.1. All computation for SRR was done through MATLAB R2022a (MathWorks, Natick, MA, USA).

SRR

The images were modeled based on $Y_k = D_k B_k G_k X + E_k$, $k = \{1 \dots N\}$, where $\{Y_k\}_N^{k-1}$ is the sets of LR images (6,12,18). D_k is the decimation operator, set based upon the decrease in spatial resolution from an HR estimate (X) to the LR Y_k . B_k is the blur operator, which is based on the point spread functions of the sensors within the instrumentation (11,12,18,29). G_k is the geometric transformation, which brings all the input images to the same point and, if unknown, can be determined based upon image registration (18). X is the estimated high-spatial-resolution image, and E_k is additive noise (12).

The values for G_k were known based upon the offsets used in the slice selection direction for the LR series. D_k was set based upon the

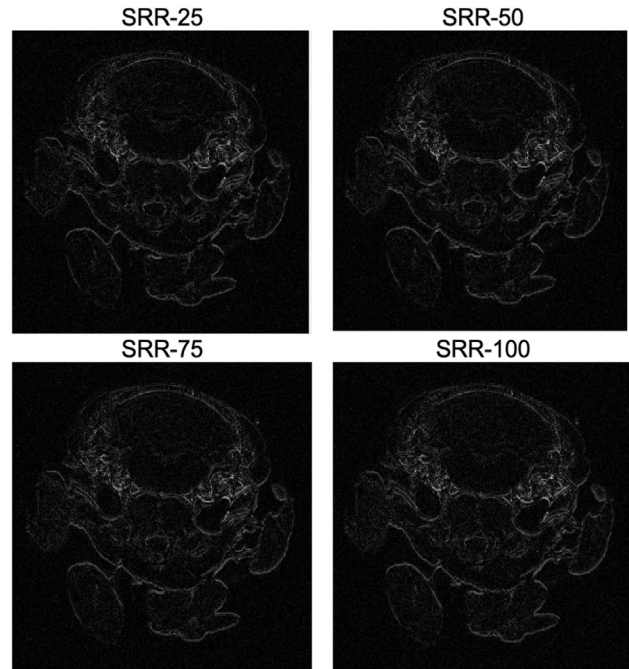


FIGURE 8 Reconstruction quality assessment of cerebellum images. The absolute difference images of the cerebellum between the high-resolution image directly acquired from the instrumentation and the reconstructed images with various offsets and number of inputs. The header signifies which reconstructed image is assessed in each image, with SRR-# indicating the offset (in micrometers) used in the low-resolution images for input.

translation from low-spatial-resolution data sets to the $100 \mu\text{m}$ isotropic data set. For SRR, the blur operator B_k is considered spatially invariant for simplicity, and the slice selection profile is often used in its place (12). However, a Gaussian function can be used to approximate the blur operator as well. For the reconstruction, the pulse profile for slice selection was modeled, and a Gaussian function was estimated that closely mimicked the excitation profile modeled. Finally, an iterative back-projection method was used to estimate the HR image and generate the SRR. The back-projection approach uses a back-projection kernel to update the current estimations of the HR reconstructions such that the LR images generated based upon the HR estimation have minimal errors between themselves and the ground-truth LR images acquired (6,12,18,29). Essentially, the back-projection kernel weights contributions from the low-spatial resolution pixels to update the current estimate of the high-resolution output until the error of the estimated and directly acquired low-resolution images,

$\sqrt{\sum_{k=1}^N (Y_k - \hat{Y}_k^n)^2}$, is minimized (6,12,18). The initial guess has been shown to have no impact on the convergence of the final solution, and for this study, an average of the low-spatial-resolution images were used to start the reconstruction (18).

TABLE 3 SNR and CNR of 2D and 3D data sets.

Dimensions of data set	SNR	CNR
2D	7.447	2.654
3D	13.035	3.375

The overall spatial resolution for both data sets was $100 \times 100 \times 300 \mu\text{m}$.

RESULTS

After reconstruction of the low-spatial-resolution archerfish image at $100 \times 100 \times 300 \mu\text{m}$ into a high-spatial-resolution image at $100 \times 100 \times 100 \mu\text{m}$, the SNR of the white matter and the CNR of the gray and white matter were determined. SNRs were determined based upon the methods suggested by NEMA (method 4) where the signal is taken from an ROI within the white matter of the brain and the noise is determined as the average noise from four ROIs outside of the sample (generally selected as the four corners of the image) and scaled by a Rayleigh distribution factor of 0.66 (30). The CNRs were determined between the gray and white matter of the brain by the differences between the signals divided by the noise (5). Compared with the directly acquired HR image, the SRR technique with a $100 \mu\text{m}$ offset yielded an increase in SNR from 6.171 to 8.487 and an increase in CNR from 5.000 to 7.428 as seen in Table 1.

The overall imaging time to acquire the HR data set was 5 h and 41 min. The LR data sets took 1 h and 53 min to acquire, per data set, leading to a total imaging time of 5 h and 39 min, a slightly depressed imaging time overall, with increased SNRs and CNRs indicated in the images seen in Figure 1.

The use of SRR to reconstruct the HR archerfish brain removed the distortion that was seen within

the LR data sets, as shown in Figure 2. While the $100 \times 100 \times 300 \mu\text{m}$ volume produces sagittal and coronal images that appear condensed to fewer slices, distorting the anatomy, the $100 \mu\text{m}$ isotropic reconstruction provides a more accurate representation of the anatomical structures in all imaging planes.

To determine the accuracy of the reconstruction, an image difference was calculated for the SRR and HR images of the archerfish. As seen in Figure 3, the image difference demonstrated the loss of noise seen as the “salt and pepper” signal along the outer edges of the image and within the brain itself. Ultimately, the reconstruction made a reasonable approximate for the high-spatial-resolution image, with the largest loss between the two images coming from noise rather than signal from true anatomical details.

The LR images of a rat brain acquired with various increments of $25 \mu\text{m}$ offsets were used to perform reconstructions with increasing numbers of image inputs to examine the impact on the number of images used in reconstruction and SNR and CNR improvements. As seen in Table 2, as the number of images used in the reconstructions increased, so did the SNRs and CNRs accordingly.

When comparing the loss between the reconstruction and the HR images, it was anticipated that as the number of LR inputs increased, the SNR would increase as the noise decreased and that the accuracy

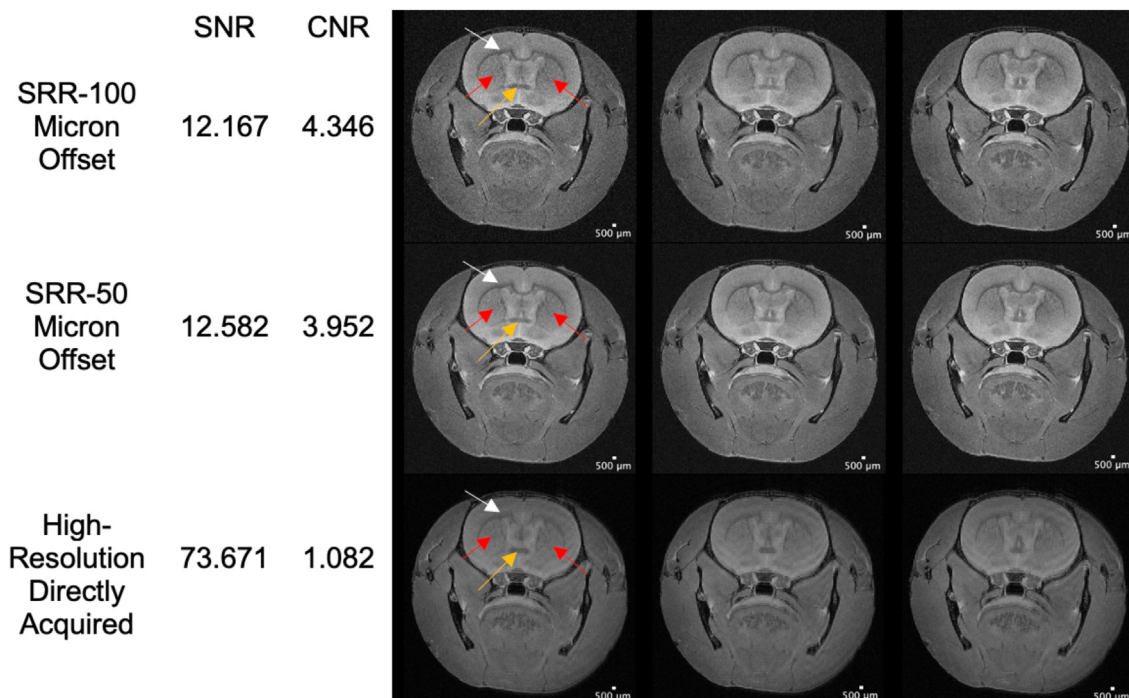


FIGURE 9 Reconstruction with 2D, $300 \mu\text{m}$ slice thickness inputs. The SNR and CNR of reconstructed images of the rat brain from a 2D low-resolution input compared with the directly acquired high-resolution image. Anatomical features are detailed with arrows with red indicating the striatum, white indicating the corpus callosum, and gold denoting the anterior commissure.

of the reconstruction would increase as well. Two different regions were chosen to examine the adherence to the HR image based upon tissue complexity for the 3D reconstructions. Figure 4 demonstrates the reconstructions and the HR comparisons for the frontal region of the brain after intensity normalization for a more accurate depiction of loss between images.

The absolute differences between the HR and reconstructed images as seen in Figure 5 demonstrate the loss of substantial noise between the reconstructed and HR images taken with only two averages. However, there was no apparent difference in the amount of loss, whether through anatomical details or noise, between the different reconstructions.

Upon closer inspection, an increase in the amount of noise lost between each of the reconstructions as the number of LR inputs increase becomes evident, which corresponds to the increasing SNR and CNR for the reconstructions. The difference between the loss in the reconstruction with 25 μm offsets and 100 μm offsets is shown, enhanced for clarity, in Figure 6.

Similar results were seen upon comparison of cerebellar slices, as seen in Figure 7. The decreased noise in the HR image of the cerebellum allows for closer inspection of the anatomical accuracy of the reconstructions. As seen in Figure 8, the greatest difference

between the HR and reconstructed images is in the loss of noise and some edge integrity; ultimately, the reconstruction still closely adheres to the directly acquired HR images.

When performing the reconstructions with 2D LR data sets, it was immediately clear that the SNR and CNR of the LR resolution inputs were decreased in contrast to the LR data sets acquired in 3D, which would likely impact the final image clarity of the reconstructed images. The SNR and CNR of the 2D and 3D LR data sets with a total spatial resolution of $100 \times 100 \times 300 \mu\text{m}$ are seen in Table 3.

After reconstruction, the impact of utilizing 2D LR inputs for the reconstruction was shown to decrease the overall achievable SNR compared with a directly acquired HR image. However, the CNR was still increased in the reconstruction compared with the directly acquired image, as seen in Figure 9. The images were reconstructed with LR data sets of $100 \times 100 \times 300 \mu\text{m}$ with either a 100 μm offset for a three-image input in the reconstruction or a 50 μm offset for a six-image input reconstruction to a $100 \times 100 \times 100 \mu\text{m}$ HR image.

Finally, after reconstruction with varying ratios between LR inputs and HR construction, the general findings indicated that the reconstruction began to suffer

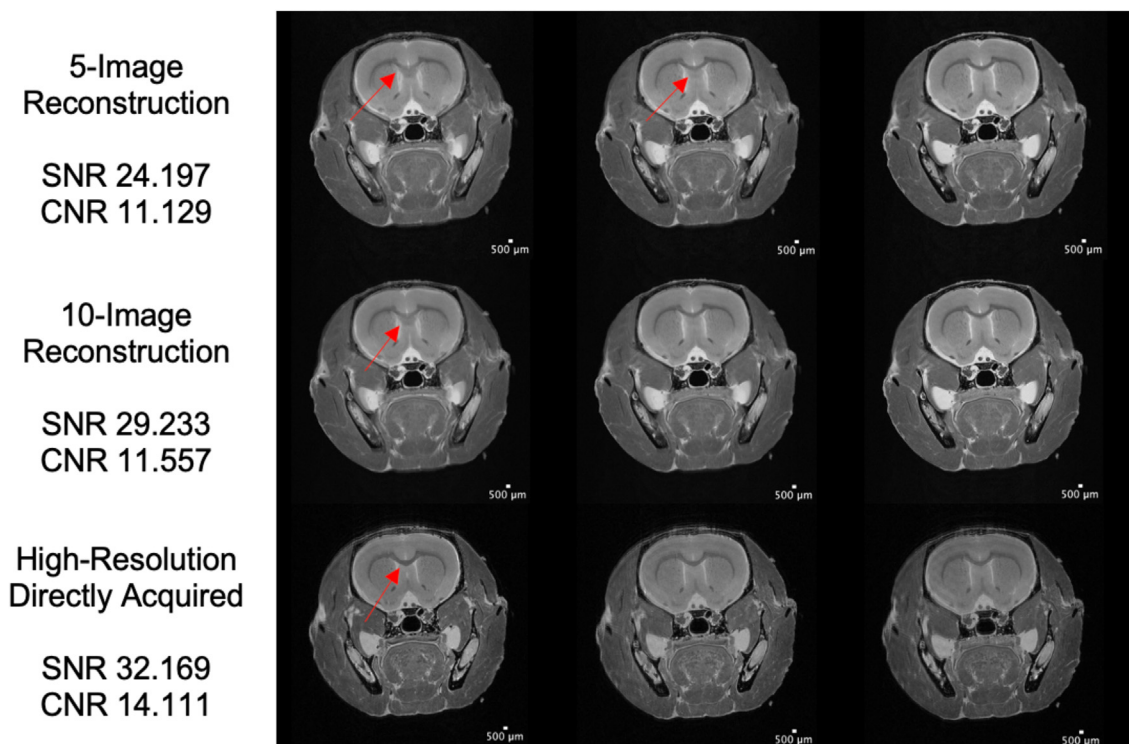


FIGURE 10 Increasing slice thickness for low-resolution inputs to 500 μm . Reconstruction with $100 \times 100 \times 500 \mu\text{m}$ low-resolution data sets using 5 images with a 100 μm offset and 10 images with a 50 μm offset compared with a directly acquired high-resolution image with 100 μm isotropic resolution. The partial volume effect is most readily seen in the corpus callosum denoted by red arrows in the first slice.

from partial volume effects at 1:4, which increased dramatically at 1:5 and 1:6. This indicates that the ideal ratio between LR inputs and HR reconstructions falls somewhere in the 1:3 and 1:4 region. At 1:2 ratios between LR and HR images, the time enhancements are not sufficient to prevent direct acquisition compared with utilization of the SRR technique. [Figure 10](#) demonstrates the partial volume effects that decrease the accuracy of the reconstruction with a 1:5 ratio of LR input/HR reconstruction.

Due to the 300, 600, 400, and 500 μm slice thickness data sets having differing corresponding HR image comparisons, separate comparisons of image loss between the HR and LR images were needed. [Figure 11](#) illustrates the comparison between the HR images directly acquired and the reconstructions using LR inputs with a slice thickness of 300 and 600 μm .

While the retention of noise is readily seen in reconstructions with a 100 μm offset from analysis of the raw data sets, the image differences reveal the divergence from the HR scans when LR inputs with 600

μm slice thickness are used. [Figure 12](#) demonstrates the loss of anatomical information from a reconstruction with larger slice slabs.

Inspection of the directly acquired HR image against the image reconstructed with LR data sets containing slice thicknesses of either 400 or 500 μm , as seen in [Figure 13](#), demonstrate a more substantial deviation from the directly acquired image as the LR inputs become larger.

Upon analysis of the absolute difference in images between the reconstruction and HR data set directly acquired, divergence from the true anatomical structure can be seen. [Figure 14](#) illustrates the regions of differences between the HR image directly acquired and reconstructions.

DISCUSSION

[Figure 15](#) shows the initial images across three slices for the HR image obtained directly and one of the LR images that correlates with the starting image for the HR

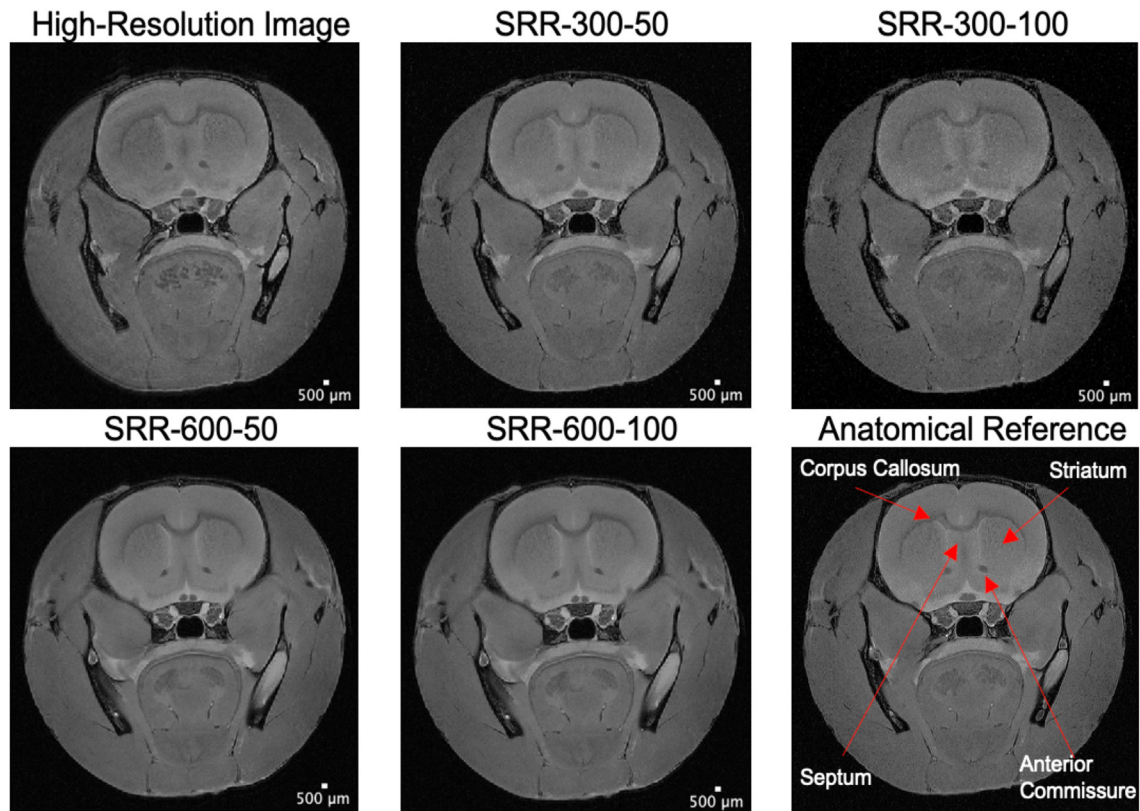


FIGURE 11 The high-resolution image at 100 μm^3 and the reconstructed images corresponding to the directly acquired image. The header above each image denotes the image type, high-resolution or super-resolution reconstruction (SRR), followed by the slice thickness of the low-resolution images used in the reconstruction (300 or 600 μm) and the offset of the low-resolution images (50 or 100 μm). The images reconstructed with a 100 μm offset present with more noise compared with those reconstructed with a 50 μm offset. The difference in noise between reconstructions is most notable in images SRR-300-50 and SRR-300-100. The images reconstructed from low-resolution inputs with a slice thickness of 600 μm demonstrate a softness to the anatomical features such as the corpus callosum and distorted anterior commissure due to partial volume effects.

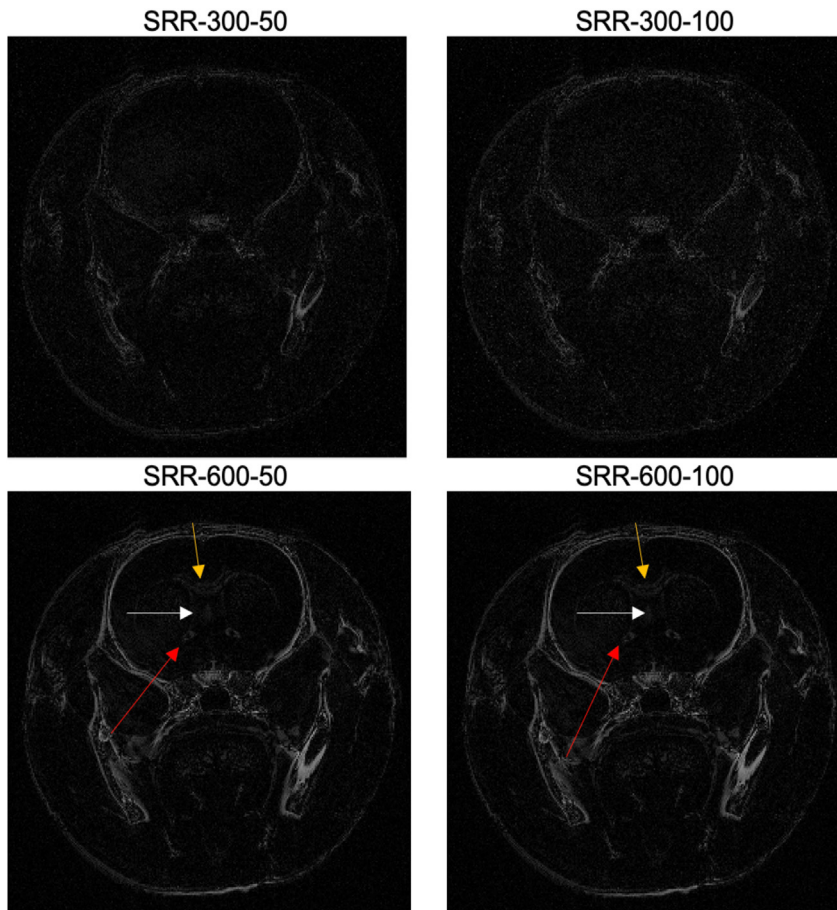


FIGURE 12 Absolute image differences of the reconstructed images and the high-resolution images. The headers denote the SRR slice thickness in μm of the low-resolution inputs and the offsets of the low-resolution data set. The reconstructions from the low-resolution data sets with a slice thickness of $300\ \mu\text{m}$ detail the difference of random white noise between the reconstructed images and the high-resolution comparison. However, the reconstruction with a slice thickness of $600\ \mu\text{m}$ presents with differences in anatomical detail denoted by the arrows. In particular, both reconstructions (SRR-600-50 and SRR-600-100) demonstrate differences in the corpus callosum (gold arrow), septum (white arrow), and anterior commissure (red arrow).

data set and the following three slices afterward. The LR images have a higher SNR due to the greater level of signal encapsulated within each voxel but suffer from partial volume effects and have greater variation between slices, which makes it difficult to get accurate assessments of the brain architecture for small samples. It was possible to reconstruct the HR image to have reasonable agreement with the directly acquired HR data with a minimal number of LR data sets to work from (three). The SNR and CNR for the directly acquired images were 6.171 and 5, while the SNR and CNR for the reconstructed images were 8.487 and 7.428. This is predicted to be a smaller improvement for the SNR compared with reconstruction with a greater volume of LR data sets. However, as an initial introduction to SRR, the results demonstrated promising results of closely matching ground-truth data through iterative back-projection methods with reasonable increases in not only the SNR but also the CNR for the final images. Overall, the SNR for the HR images acquired directly was lower and the images took longer to acquire than the reconstructed HR data set, indicating SRR as an advantageous method for clinical and research applications using MR technology.

The use of 12 images acquired with a $25\ \mu\text{m}$ slice offset allowed for the reconstruction with three images at a $100\ \mu\text{m}$ offset, four images at $75\ \mu\text{m}$, six images at $50\ \mu\text{m}$, and 12 images with a $25\ \mu\text{m}$ offset to determine how greatly the number of starting LR images influences the HR reconstruction. The reconstructions were performed using the same method outlined previously with iterative back projection. Figure 16 shows the reconstructed images for the varying number of LR sets used in the reconstruction and the corresponding effect on the SNR and CNR. As the number of LR inputs increased, so did the SNR and CNR, although there is decreased benefit in going from six to 12 LR inputs. However, the original HR data set directly acquired had an SNR greater than 70, indicating that for larger sample sizes, which will be adequately sized for the probe used during imaging, SRR may not give comparable SNR measurements to direct acquisition, although the CNR of 1.08 indicates that SRR gives better intensity separation between tissues. Ultimately, for the experimental parameters listed above, an HR data set acquired with 12 averages (akin to using 12 LR images in the reconstruction) will take a total of 3234 min to acquire

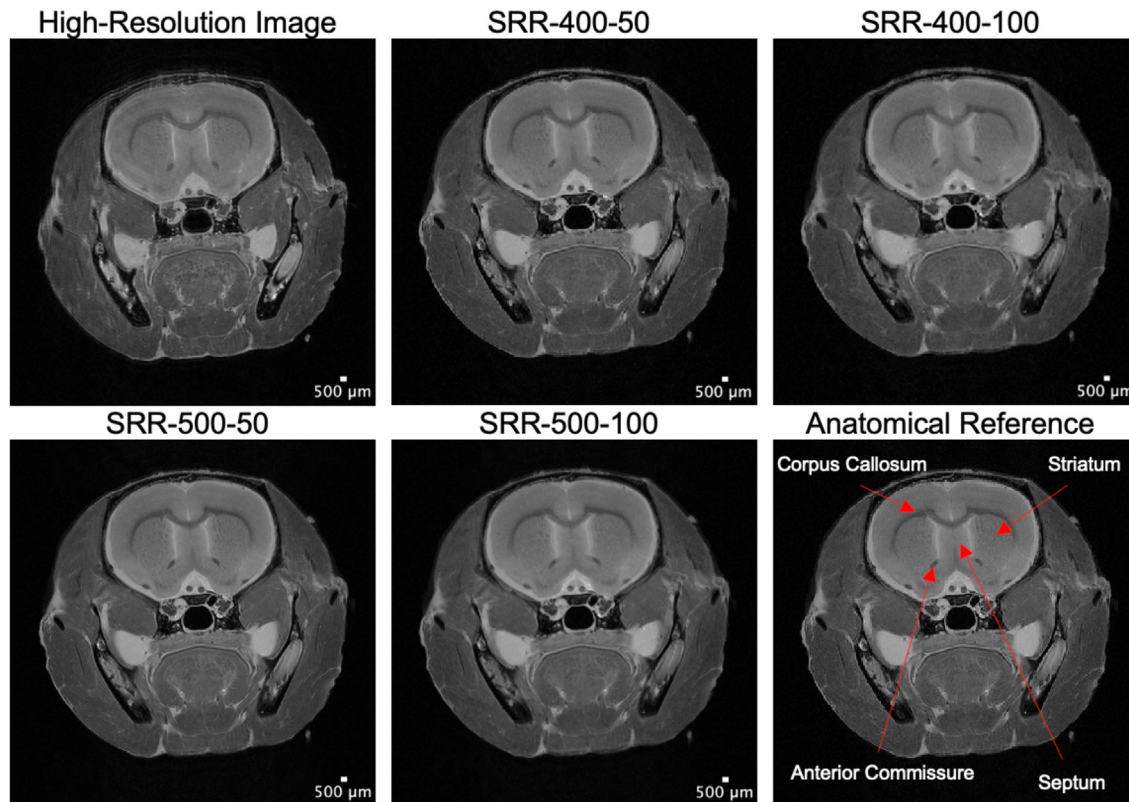


FIGURE 13 Reconstructions from low-resolution inputs of 400 and 500 μm slice thickness. Image comparison between the high-resolution image directly acquired and the reconstructed image with low-resolution data sets with slice thickness of either 400 or 500 μm for low-resolution inputs. The header above each image denotes whether it is the original or SRR image, followed by the slice thickness used in the low-resolution inputs, and finally the offset in μm of each low-resolution data set. The reconstructed images begin to deviate more substantially from the directly acquired high-resolution image due to insufficient information in each low-resolution data set and insufficient numbers of low-resolution inputs.

compared with 1078 min for the total acquisition of the LR data sets, indicating that to condense imaging time, it may be worth the SNR trade-off to utilize SRR compared with direct acquisition due to imaging time constraints. It is important to mention that these metrics are given based upon 3D imaging techniques, which take longer due to the additional spatial encoding for each slice; with 2D image acquisition for the LR data sets, this time difference becomes even more pronounced.

The same iterative back-projection technique was used to reconstruct the HR images from 2D LR inputs. While reconstructions with 2D data sets do not demonstrate the same increase in SNRs compared with the 3D LR data sets, they still produce greater CNRs than the directly acquired HR images. The CNR is a key parameter in MRI, and imaging parameters are often focused on acquiring the highest CNRs possible, thus the increase in the CNR still indicates an asset to SRR even with noisier LR basis sets. Additionally, the SNR efficiency for the SRR for the 100 μm offset reconstruction was 0.449 compared with

0.354 for the HR directly acquired, indicating a greater efficiency for the SRR reconstruction with a total imaging time of 20 min and 30 s for the LR data sets to perform SRR with 50 μm offsets, while the HR data set acquired directly with 12 averages took over 25 h.

Figure 17 demonstrates the LR images across three slices and the directly acquired HR image. While the images start at comparable slices, the LR with 600 μm slice thickness clearly starts slightly before the directly acquired HR data set and ends after the HR data set. For the LR sets with 400 and 500 μm slice thicknesses, this difference is less noticeable but can be seen in the last slice, where the corpus callosum starts to reach further down and the anterior commissure is closer together compared with the directly acquired HR data sets. The initial SNRs for the LR data sets show an increase as slice thickness increases (which is to be expected). For comparison, the 300 μm LR data set had an SNR and CNR of 7.447 and 2.654. With a 100 μm jump to a slice thickness of 400 μm , the SNR and CNR increase to 16.829

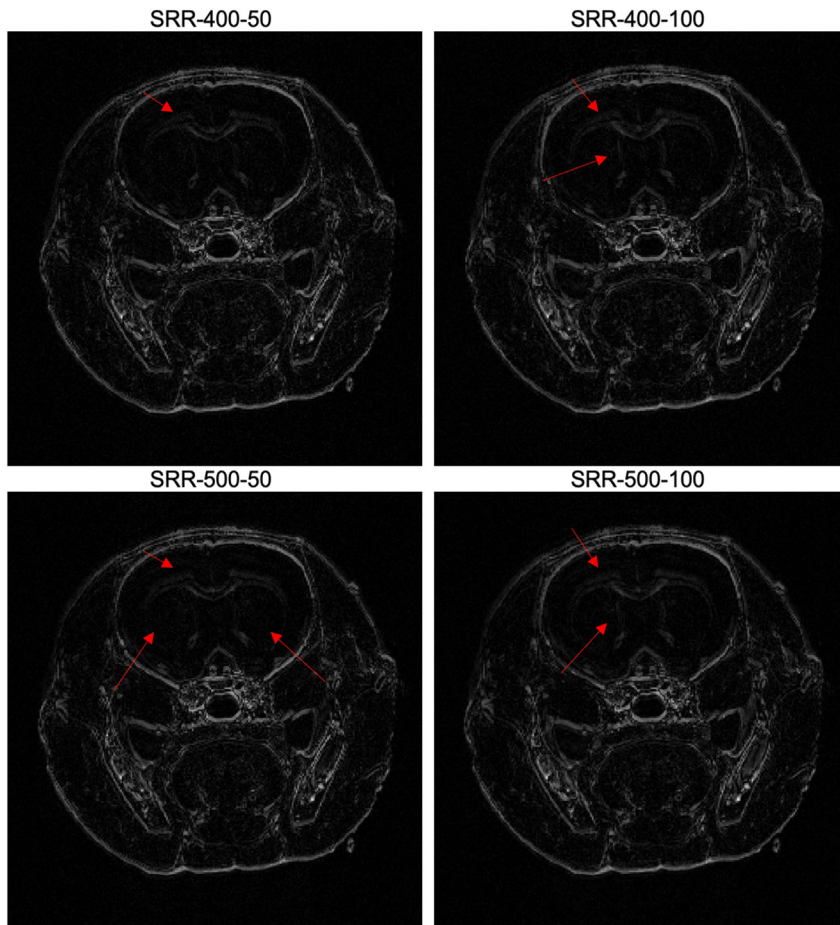


FIGURE 14 Images denoting the differences between the high-resolution images directly acquired and those reconstructed with various low-resolution inputs. While first glance of the images showed little difference between the reconstruction and the high-resolution image directly acquired, the image differences calculated reveal regions that were incorrectly estimated such as the corpus callosum and regions around the septum. Red arrows denote key areas of divergence from the high-resolution scan. Image headers denote the SRR, the slice thickness of the low-resolution input, and the offset between each low-resolution data set.

and 7.345, and at 500 μm , these measurements are 19.490 and 6.581. The SNR of the 600 μm slice thickness was less impressive (17.093) but maintained a high CRN of 7.599. The decreased SNR could be due to trying to keep the TR/TE comparable to the matching HR data set that was used for comparison in a separate trial.

Reconstructions with each LR data set were performed with 50 and 100 μm offsets. Figure 18 demonstrates the SRR with four LR images with a slice thickness of 400 μm and a 100 μm offset and eight LR images with a 50 μm offset compared with the HR image directly acquired. While the first two images show good coherence with the directly acquired HR image, at the third slice, the reconstructions show a lack of intensity and more spread of the signal as the conformation of the corpus callosum changes. This is less severe in the 50 μm offset reconstruction but still shows deviation from the directly acquired HR image. Additionally, there is no increase in the SNR or CNR for a four-image reconstruction with 100 μm offsets in the through-plane dimension. However, the eight image, 50 μm offset reconstruction does offer

comparable SNRs and subtle increases in CNRs compared with those of the directly acquired HR data set.

Unfortunately, with a 5:1 reconstruction between the HR and LR data sets, the reconstructions started to diverge from the directly acquired reference point. Reconstructions with LR data sets show divergence along the corpus callosum within the first slice, demonstrated in Figure 10, where the new information contained within each successive offset is not substantial enough/does not contribute enough to the next offset image for robust reconstruction. Additionally, at this reconstruction ratio, the SNR and CNR benefits are no longer consistent compared with what had been seen with previous reconstructions with 3:1 and 4:1 ratios between LR and HR data sets. This divergence from the directly acquired image is exacerbated by the 6:1 ratio between LR and HR data sets, as seen in Figure 19. While the SNR in the reconstructions is quite promising, the solution for the SRR fails to identify a solid boundary for the skull, causing a diffusive signal around the brain. This continues with a failure to adequately follow the changes in the corpus

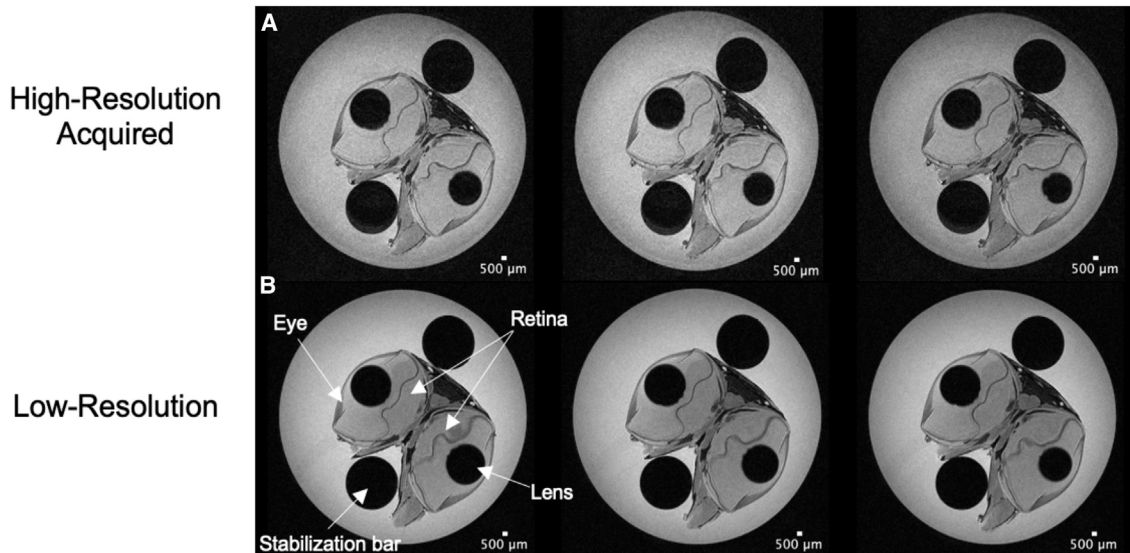


FIGURE 15 High- and low-resolution images of the archerfish. High-resolution images of the archerfish (row A) compared with low-resolution images (row B) across three slices demonstrate the increased noise seen in the high-resolution image directly acquired and the predisposition to partial volume effects seen in the low-resolution image. The noise is most prevalent in the background of the high-resolution images, and the partial volume effects are best seen in the vasculature of the eyes in the low-resolution scans. Anatomical markers detail the eye, vasculature of the eye, retina, and stabilization bars, which were used to secure the sample in the imaging tube.

callosum across slices. However, much like in the other reconstructions, increasing the number of LR inputs in the reconstruction minimizes the decoherence between the directly acquired and reconstructed images, as can be seen in the 12- vs. six-image reconstruction, yet the practicality decreases as the ratio between the LR and HR data sets increases, and thus the total number of LR data sets that would need to be acquired become burdensome. Ultimately, it seems that for optimal reconstructions, the HR images to be reconstructed should be no more than four times the resolution of the LR data sets used to reconstruct them, with 3:1 offering the best results.

Overall, our results indicate that SRR produces images that closely mirror their directly acquired HR counterparts with greater SNR efficiency, thereby enabling HR data sets to be achieved in condensed time frames. In cases where the sample did not occupy the maximal amount of space in the imaging

probe, such as the archerfish, the SNR and CNR were greater than those of the directly acquired HR images. It was anticipated that as the number of LR inputs used in the reconstruction increased, the SNR and CNR would increase for all sample types; however, that was not the case. While the SNR and CNR increased as the number of LR inputs increased, they did not surpass that of the directly acquired HR images for the rat brain samples, although they were fairly close in some trials. SRR may have a more significant effect on the SNR in smaller samples, which do not sufficiently occupy probe space, leaving a larger gap between the sample and the transmit and receiver coils due to the increase in background noise, which is largely removed with SRR strategies.

While the rat brain samples did not see as much improvement in the SNR with the reconstruction technique, there was an increase in the CNR compared with the directly acquired HR images. This may still

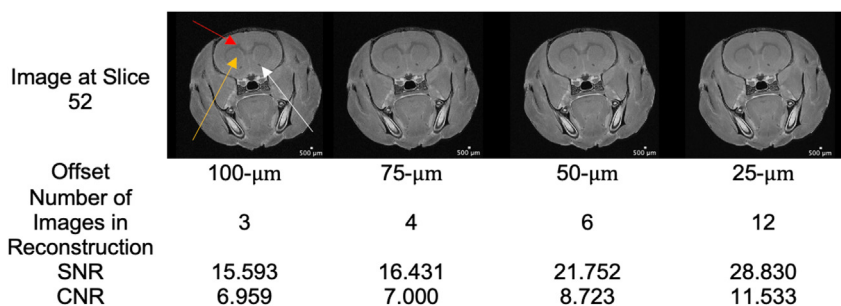


FIGURE 16 Impact of increase image inputs for reconstruction. Reconstructed images with decreasing offsets and increasing number of low-resolution inputs demonstrating a slight decrease in visible noise, increase in image sharpness, and increasing SNR and CNR as the number of low-resolution inputs increase. In the first image on the left, regions of the corpus callosum (red arrow), striatum (gold arrow), and anterior commissure (white arrow) are denoted as anatomical landmarks.

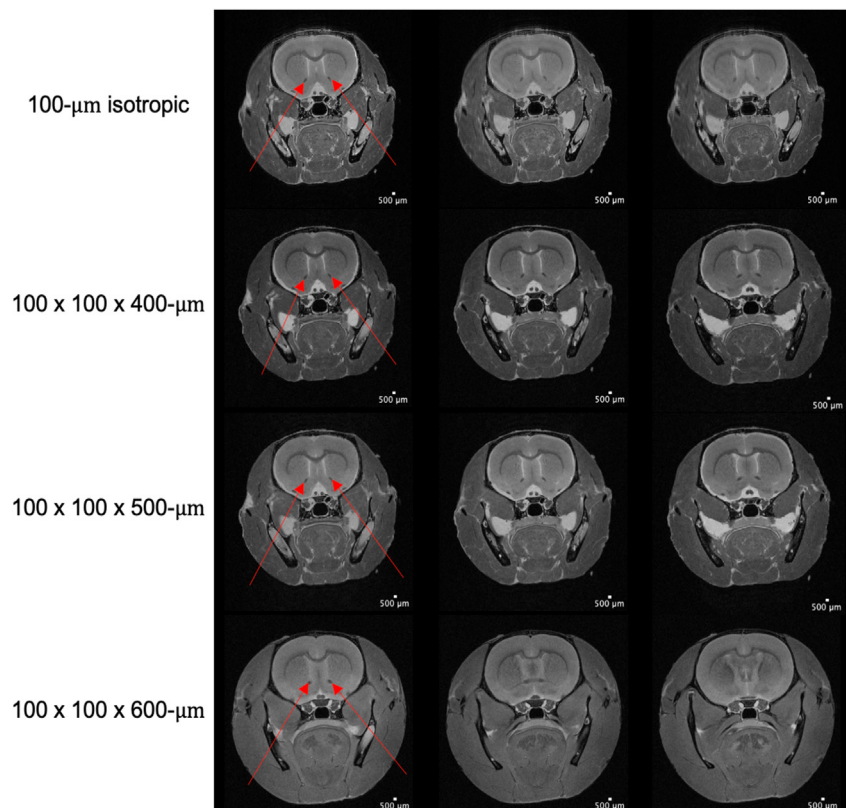


FIGURE 17 High- and low-resolution images of the rat brain at comparable slice locations. Directly acquired high-resolution 100 μm isotropic image compared with low-resolution data sets across three slices with varying slice thicknesses. Anterior commissures are highlighted with red arrows in the first slice of each image series for anatomical reference. As the slice thickness for the low-resolution input increases, the prevalence of the partial volume effect increases, and the anatomical change within each slices increases as well based upon slice location.

produce enough benefit to utilize SRR over direct acquisition at ultrahigh fields, as the CNR is an important characteristic in MRI for defining tissue boundaries. Additionally, 2D LR data sets, in general, can be generated rapidly in minutes and may present with enough of a cost benefit to utilize reconstruction over direct acquisition. Therefore, image reconstruction to HR data sets, otherwise inaccessible due to instrument strengths or time, may provide ultra-HR imaging to more locations and for more applications once thoroughly investigated for limitations. The reconstruction algorithm is a quick and efficient and can provide the HR output in minutes, which closely mirrors what could be obtained directly at ultrahigh fields. Based upon these findings, SRRs could present a unique opportunity in clinical settings to achieve ultrahigh resolution even at lower field strengths, providing radiologists with more detailed information during patient assessments.

CONCLUSIONS

SRR is an innovative method to increase the spatial resolution of MRIs without suffering from a decreased signal, which is a frequent side effect of acquiring ultrahigh-spatial-resolution images directly. In this project, reconstructions of HR images from both 2D and 3D LR data sets were obtained through a series of experi-

ments. It has been demonstrated that an increase in the SNR is sample dependent, but reasonably high SNRs can be achieved with reconstruction equivalent to or surpassing that achieved from HR imaging directly at ultrahigh fields, but with the benefit of decreased acquisition times. Furthermore, reconstructions with 2D data sets demonstrated that imaging time could be dramatically reduced while increasing the CNR of the reconstructed images compared with their directly acquired HR counterparts. Although reconstruction with 2D LR data sets does not produce the same pronounced increase in the SNR upon reconstruction as was seen with 3D imaging, the SNRs were comparable to most of the HR images directly acquired. Additionally, our results indicate that the impact on the number of LR data sets used in the reconstructions has a profound impact on the reconstructed image SNR and CNR, which increase as the number of LR inputs increase. However, for the overall time of data acquisition for SRR to remain a cost-effective option, the total number of LR data sets should be restricted. Given that the most substantial signal-to-noise improvements are apparent at six LR inputs for reconstruction, this may provide a reasonable minimum for rigorous reconstructions. We also investigated the upper limits for through-plane resolution for the LR inputs and found that a 1:3 ratio between HR and LR data is optimal for reconstruction and yields

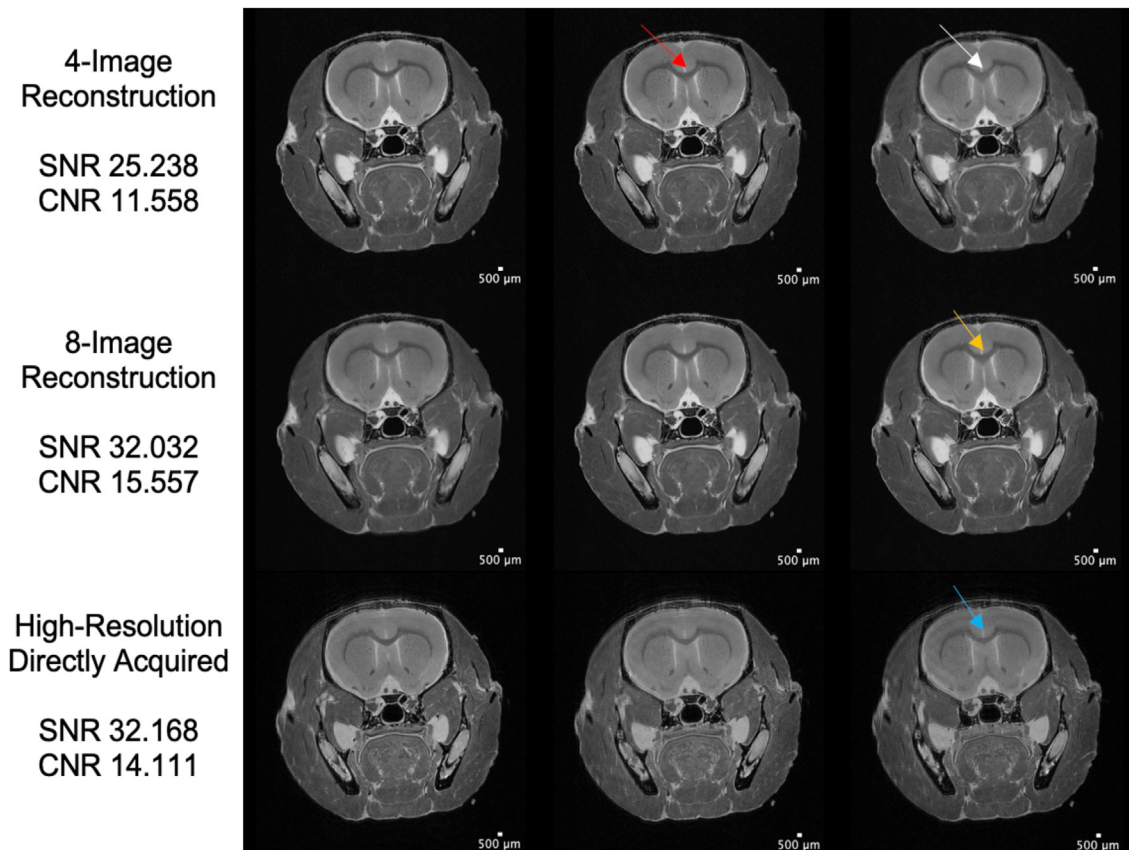


FIGURE 18 SRR with $100 \times 100 \times 400 \mu\text{m}$ low-resolution images to reconstruct the high-resolution $100 \times 100 \times 100 \mu\text{m}$ images. The top three images depict a reconstruction with low-resolution inputs at a $100 \mu\text{m}$ offset and show divergence from the high-resolution image directly acquired. This is most noticeable at the corpus callosum shown via the white arrow compared with the blue arrow in the high-resolution image. The reconstruction provides a better estimate in the previous slice shown with the red arrow. The second set of three images demonstrate the reconstruction with a $50 \mu\text{m}$ offset and show a better approximation of the corpus callosum (gold arrow) when referenced against the directly acquired high-resolution scans, indicating that as the number of low-resolution inputs increase, the estimate becomes more accurate, even with larger low-resolution slice selections.

the greatest agreement between reconstructed and directly acquired HR data. However, 1:4 ratios between the HR and LR images may be sufficient so long as the ROIs have larger boundaries between tissues and easily defined contrast changes between ROIs. Reconstructed images were carefully examined and compared against directly acquired HR data acquired with multiple averages (to maintain high SNRs) to ascertain the accuracy of reconstructions against a variety of landmarks such as the corpus callosum and anterior commissure. Ultimately, we consider SRR an effective strategy to increase image spatial resolution while condensing imaging time, and it may prove useful in clinical and research settings to maintain patient comfort, assess greater ROIs or additional metrics (such as diffusion imaging) in live animal imaging, improve SNRs and CNRs at lower field strengths, and obtain more useful images for samples that do not adequately fill the radiofrequency coil and thus are predisposed to increased noise.

The strategy of SRR will provide a means of investigating ultrahigh anatomical detail in a time-efficient manner. This will allow for rapid dissemination of information for areas of comparative neuroscience and brain research by allowing for rapid imaging while maintaining ultrahigh resolutions. With more rigorous testing and verification against HR images directly acquired, this method can be applied to alternative pulse sequences and imaging strategies to include quantitative forms of MRI as well. This will allow for more frequent *in vivo* work, as anesthesia time is often a limiting factor in imaging. In doing so, it will provide more avenues for in-depth understanding of neural connections and disease progressions.

SUPPORTING MATERIAL

Supplemental information can be found online at <https://doi.org/10.1016/j.bpr.2023.100107>.

6 -Image Reconstruction

SNR 31.354
CNR 10.043

12-Image Reconstruction

SNR 32.541
CNR 11.804

High-Resolution Acquired

SNR 73.671
CNR 1.082

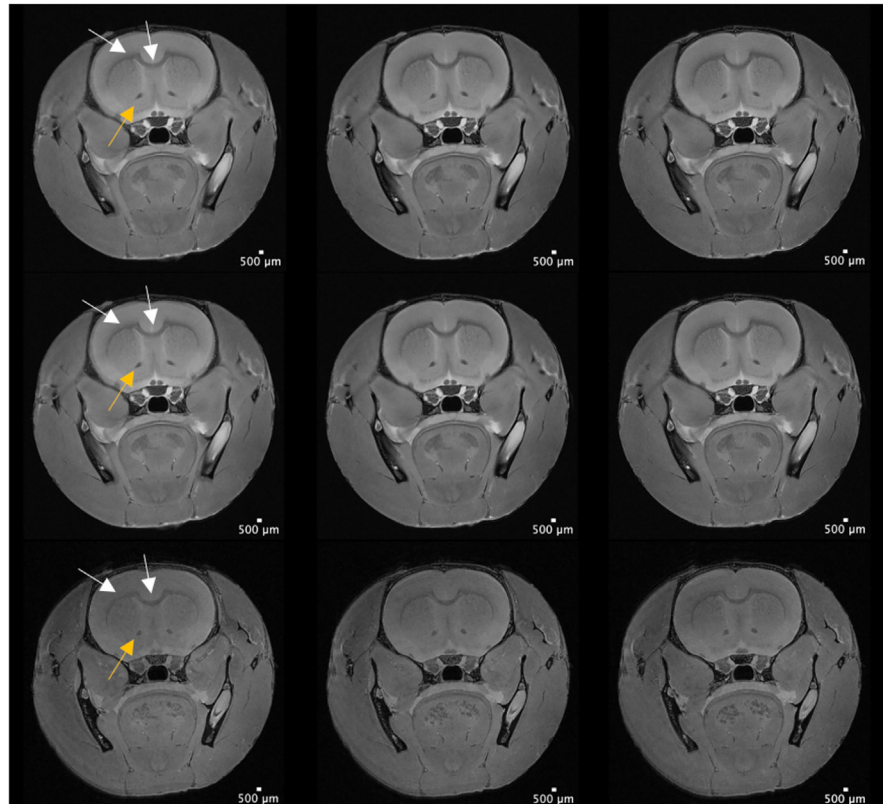


FIGURE 19 Image reconstructions from low-resolution inputs with $600 \mu\text{m}$ slice thickness. Comparison of a directly acquired high-resolution data set with reconstructions with low-resolution data sets of $100 \times 100 \times 600 \mu\text{m}$ with six or 12 images and a 100 or $50 \mu\text{m}$ offset. The reconstructions illustrate a divergence from the directly acquired high-resolution image and a lack of tissue definition. This is most apparent in the six-image reconstruction with the corpus callosum shown via white arrows and the anterior commissure shown with gold arrows when compared with the high-resolution image. While there is improvement as the number of low-resolution inputs increase as seen in the 12-image reconstruction, the high-resolution estimate is not sufficient.

AUTHOR CONTRIBUTIONS

Conceptualization, writing, and software, S.H.B. and M.P.; validation, supervision, resources, and funding, S.H.B.; data analysis, M.P.; data acquisition and curation, I.M. and M.P.; resources, M.C.; resources and writing, T.M. and R.S. All authors reviewed and edited the manuscript.

ACKNOWLEDGMENTS

The authors acknowledge financial support from NIH R01EB028848 (Treating Primary aldosteronism-induced hypertension via microwave thermal therapy; Punit Prakash (PI), Stefan H. Bossmann (MPI)).

DECLARATION OF INTERESTS

The authors declare no competing interests.

REFERENCES

1. van Osch, M. J. P., and A. G. Webb. 2014. Safety of Ultra-High Field MRI: What are the Specific Risks? *Curr. Radiol. Rep.* 2:61.
2. Kangarlu, A., R. E. Burgess, H. Zhu, T. Nakayama, R. L. Hamlin, A. M. Abduljalil..., 1999. Cognitive, cardiac, and physiological safety studies in ultra high field magnetic resonance imaging. *Magn. Reson. Imaging.* 17:1407–1416.
3. Sadeghi-Tarakameh, A., L. DelaBarre, R. L. Lagore, A. Torrado-Carvajal, X. Wu, A. Grant, G. Adriany, G. J. Metzger, P. Van de Moortele, K. Ugurbil, E. Atalar, and Y. Eryaman. 2020 Jul 1. In vivo human head MRI at 10.5T: A radiofrequency safety study and preliminary imaging results. *Magn. Reson. Med.* 84:484–496.
4. Allisy-Roberts, P., and J. Williams. 2007. *Farr's Physics for Medical Imaging*, 2nd ed. Saunders Ltd.
5. McRobbie, D. W., E. A. Moore, M. J. Graves, and M. R. Prince. 2006. *MRI From Picture to Proton*. Cambridge university press.
6. Carmi, E., S. Liu, N. Alon, A. Fiat, and D. Fiat. 2006. Resolution enhancement in MRI. *Magn. Reson. Imaging.* 24:133–154.
7. Farsiu, S., M. D. Robinson, M. Elad, and P. Milanfar. 2004. Fast and robust multiframe super resolution. *IEEE Trans. Image Process.* 13:1327–1344.
8. Miloshev, V. Z., K. Deh, and K. R. Keshari. 2022. Free super-resolution MRI by BRICKD slices. *J. Magn. Reson.* 341:107246.
9. Bai, Y., X. Han, and J. L. Prince. 2004. Super-resolution Reconstruction of MR Brain Images. *In Proceedings of 38th annual conference on information sciences and systems*, pp. 1358–1363.

10. Park, S. C., M. K. Park, and M. G. Kang. 2003. Super-resolution image reconstruction: A technical overview. *IEEE Signal Process. Mag.* 20:21–36.
11. Reeth, E van, I. W. K. Tham, C. Heng Tan, and C. Loo Poh. 2012. Super-Resolution in Magnetic Resonance Imaging: A Review. *Concepts Magn. Reason. A.* 40:306–325.
12. Greenspan, H., G. Oz, N. Kiryati, and S. Peled. 2002. MRI interslice reconstruction using super-resolution. *Magn. Reason. Imaging.* 20:437–446.
13. Peeters, R. R., P. Kornprobst, M. Nikolova, S. Sunaert, T. Vieville, G. Malandain, R. Deriche, O. Faugeras, M. Ng, and P. Van Hecke. 2004. The use of super-resolution techniques to reduce slice thickness in functional MRI. *Int. J. Imaging Syst. Technol.* 14:131–138.
14. Gholipour, A., J. A. Estroff, and S. K. Warfield. 2010. Robust super-resolution volume reconstruction from slice acquisitions: Application to fetal brain MRI. *IEEE Trans. Med. Imaging.* 29:1739–1758.
15. Sarasaen, C., S. Chatterjee, M. Breitkopf, G. Rose, A. Nürnberger, and O. Speck. 2021. Fine-tuning deep learning model parameters for improved super-resolution of dynamic MRI with prior-knowledge. *Artif. Intell. Med.* 121:102196.
16. Zhu, X., L. Sun, Y. Chen, Z. Ye, Z. Shen, and G. Li. 2013. A pixel is an artifact: on the necessity of zero-filling in Fourier imaging. *Biosens. Bioelectron.* 47:32–37.
17. Bernstein, M. A., S. B. Fain, and S. J. Riederer. 2001. Effect of Windowing and Zero-Filled Reconstruction of MRI Data on Spatial Resolution and Acquisition Strategy. *J. Magn. Reson. Imaging.* 14:270–280.
18. Irani, M., and S. Peleg. 1991. Improving Resolution by Image Registration. *CVGIP Graph. Models Image Process.* 53:231–239.
19. Mufti, N., M. Ebner, P. Patel, M. Aertsen, T. Gaunt, P. D. Humphries, F. E. Bredaki, R. Hewitt, C. Butler, M. Sokolska, G. S. Kendall, D. Atkinson, T. Vercauteren, S. Ourselin, P. P. Pandya, J. Deprest, A. Melbourne, and A. L. David. 2021. Super-resolution Reconstruction MRI Application in Fetal Neck Masses and Congenital High Airway Obstruction Syndrome. *OTO Open.* 5:2473974X211055372.
20. Cozzi, J., A. Fraichard, and K. Thiam. 2008. Use of genetically modified rat models for translational medicine. *Drug Discov. Today.* 13:488–494.
21. Homberg, J. R., M. Wöhr, and N. Alenina. 2017. Comeback of the Rat in Biomedical Research. *ACS Chem. Neurosci.* 8:900–903.
22. Calabrese, E., A. Badea, C. Watson, and G. A. Johnson. 2013. A quantitative magnetic resonance histology atlas of postnatal rat brain development with regional estimates of growth and variability. *Neuroimage.* 71:196–206.
23. Sergejeva, M., E. A. Papp, R. Bakker, M. A. Gaudnek, Y. Okamura-Oho, J. Boline, J. G. Bjaalie, and A. Hess. 2015. Anatomical landmarks for registration of experimental image data to volumetric rodent brain atlasing templates. *J. Neurosci. Methods.* 240:161–169.
24. Kjonigsen, L. J., S. Lillehaug, J. G. Bjaalie, M. P. Witter, and T. B. Leergaard. 2015. Waxholm Space atlas of the rat brain hippocampal region: Three-dimensional delineations based on magnetic resonance and diffusion tensor imaging. *Neuroimage.* 108:441–449.
25. Paxinos, G., and C. Watson. 2006. *The Rat Brain in Stereotaxic Coordinates*, 6th ed. Academic Press.
26. Karoubi, N., R. Segev, and M. F. Wullimann. 2016. The Brain of the Archerfish *Toxotes chatareus*: A Nissl-Based Neuroanatomical Atlas and Catecholaminergic/Cholinergic Systems. *Front. Neuroanat.* 10:106.
27. Ben-Tov, M., O. Ben-Shahar, and R. Segev. 2018. What a predator can teach us about visual processing: a lesson from the archerfish. *Curr. Opin. Neurobiol.* 52:80–87.
28. Newport, C., G. Wallis, and U. E. Siebeck. 2014. Concept learning and the use of three common psychophysical paradigms in the archerfish (*Toxotes chatareus*). *Front. Neural Circuits.* 8:39.
29. Irani, M., and S. Peleg. 1993. Motion Analysis for Image Enhancement: Resolution, Occlusion, and Transparency. *J. Vis. Commun. Image Represent.* 4:324–335.
30. NEMA Standards Publication MS 1-2008 (R2014, R2020) Determination of Signal-to-Noise Ratio (SNR) in Diagnostic Magnetic Resonance Imaging. (2021). www.nema.org